



# All-organic heterojunctions used for the excellent photocatalytic H<sub>2</sub>O<sub>2</sub> synthesis: The key role of bay-position Cl in PDI

Tingting Dong<sup>a</sup>, Guohui Dong<sup>a,\*</sup>, Kai Han<sup>a</sup>, Caihong Chen<sup>a</sup>, Jiwen Hu<sup>b,\*</sup>, Kajsas Uvdal<sup>b</sup>

<sup>a</sup> School of Environmental Science and Engineering, Shaanxi University of Science and Technology, Xi'an 710021, PR China

<sup>b</sup> Department of Physics, Chemistry and Biology (IFM), Linköping University, SE-58183, Sweden

## ARTICLE INFO

### Keywords:

H<sub>2</sub>O<sub>2</sub> production  
Built-in electric field  
Cl substitution  
Photocatalysis  
Melem

## ABSTRACT

Melem is the basic structural unit of g-C<sub>3</sub>N<sub>4</sub>. When directly utilized as a photocatalyst, the separation efficiency of photogenerated electron-hole pairs is low. In this study, we constructed a Melem-based all-organic heterojunction (PICN) by reacting the -NH<sub>2</sub> at the terminal of the Melem unit with the anhydride of PDA. The photocatalytic efficiency for H<sub>2</sub>O<sub>2</sub> production of the heterojunction is 4.2 times that of CN. Introducing -Cl at the bay position of PDI further enhances the photocatalytic H<sub>2</sub>O<sub>2</sub> production efficiency by 1.6 times. This enhancement is attributed to the introduction of -Cl, which not only broadens the UV-visible light absorption range of the sample but also improves the interface electron transfer efficiency between Melem and PDI-Cl. Moreover, the introduction of -Cl can also reduce the overpotential of the O<sub>2</sub> reduction reaction on the surface of the sample. These novel findings may provide insights for the design of organic heterojunction photocatalysts.

## 1. Introduction

Hydrogen peroxide (H<sub>2</sub>O<sub>2</sub>) is a high-value chemical widely used in chemical synthesis, medical disinfection, environmental and other fields. At the same time, it is also applied as a new type of green energy storage material in the fuel cell industry [1–6]. The wide application prospect drives continuous effort to seek efficient and environmentally friendly H<sub>2</sub>O<sub>2</sub> production process. To date, considerable efforts have been made to develop synthetic methods for H<sub>2</sub>O<sub>2</sub> production [7–10]. Traditional H<sub>2</sub>O<sub>2</sub> production mainly uses the anthraquinone process, reportedly constituting 95% of global H<sub>2</sub>O<sub>2</sub> production [11,12]. However, anthraquinone process often involves the use of toxic organic solvents (heavy aromatics, trioctyl phosphate), and the byproducts (CO, H<sub>2</sub>S) also show strong environmental toxicity [4,13]. This contradicts the current trend of low-carbon and environmentally friendly chemical production processes. Besides the anthraquinone process, the catalytic synthesis of H<sub>2</sub>O<sub>2</sub> by direct combination of H<sub>2</sub> and O<sub>2</sub> using precious metals faces challenges including high cost, low product selection and the risk of direct explosion of H<sub>2</sub>/O<sub>2</sub> mixture [8,14]. The synthesis of H<sub>2</sub>O<sub>2</sub> by solar driven photocatalyst is a green and sustainable production method. Using O<sub>2</sub> and H<sub>2</sub>O as raw materials, this process has the advantages of mild reaction conditions, simple and controllable operation, and zero secondary pollution. At present, many inorganic

semiconductor photocatalysts such as TiO<sub>2</sub> [15,16], ZnO [17], BiVO<sub>4</sub> [18,19] and CdS [20] can be used for the H<sub>2</sub>O<sub>2</sub> synthesis. However, metal ions released by inorganic photocatalytic materials are prone to fenton-like reactions, which further decompose hydrogen peroxide into hydroxyl free radicals [21]. Therefore, it is crucial to search for an environmentally friendly, earth-abundant non-metallic semiconductor photocatalyst.

In previous studies, conjugated microporous polymers (CMP), covalent organic frameworks (COF), and covalent triazine frameworks (CTF) have been favored by researchers for their stable and ordered framework structures, but the further application has been limited by the factors such as cost, synthesis, and toxicity [22,23]. g-C<sub>3</sub>N<sub>4</sub> is a non-toxic organic photocatalytic material with abundant sources and simple preparation process [24–26]. Melem is an important intermediate in the synthesis of g-C<sub>3</sub>N<sub>4</sub>, with strict C-N alternating skeleton and easily modified -NH<sub>2</sub>, which can construct covalently bonded heterojunction with many organic molecules, and is an excellent monomer for the preparation of non-metallic photocatalysts. For example, the researchers build organic heterojunctions and create built-in electric fields by embedding C-O-C chains, carbon rings, or carbon dopants at the edges of Melem [27–30]. In fact, the built-in electric field, as a key dynamic factor controlling carrier transport, is crucial for charge separation.

In the design of functional materials, heterogeneous structure

\* Corresponding authors.

E-mail addresses: [dongguohui@sust.edu.cn](mailto:dongguohui@sust.edu.cn) (G. Dong), [jiwen.hu@liu.se](mailto:jiwen.hu@liu.se) (J. Hu).

<https://doi.org/10.1016/j.apcatb.2024.124144>

Received 1 March 2024; Received in revised form 28 April 2024; Accepted 30 April 2024

Available online 3 May 2024

0926-3373/© 2024 Elsevier B.V. All rights reserved.

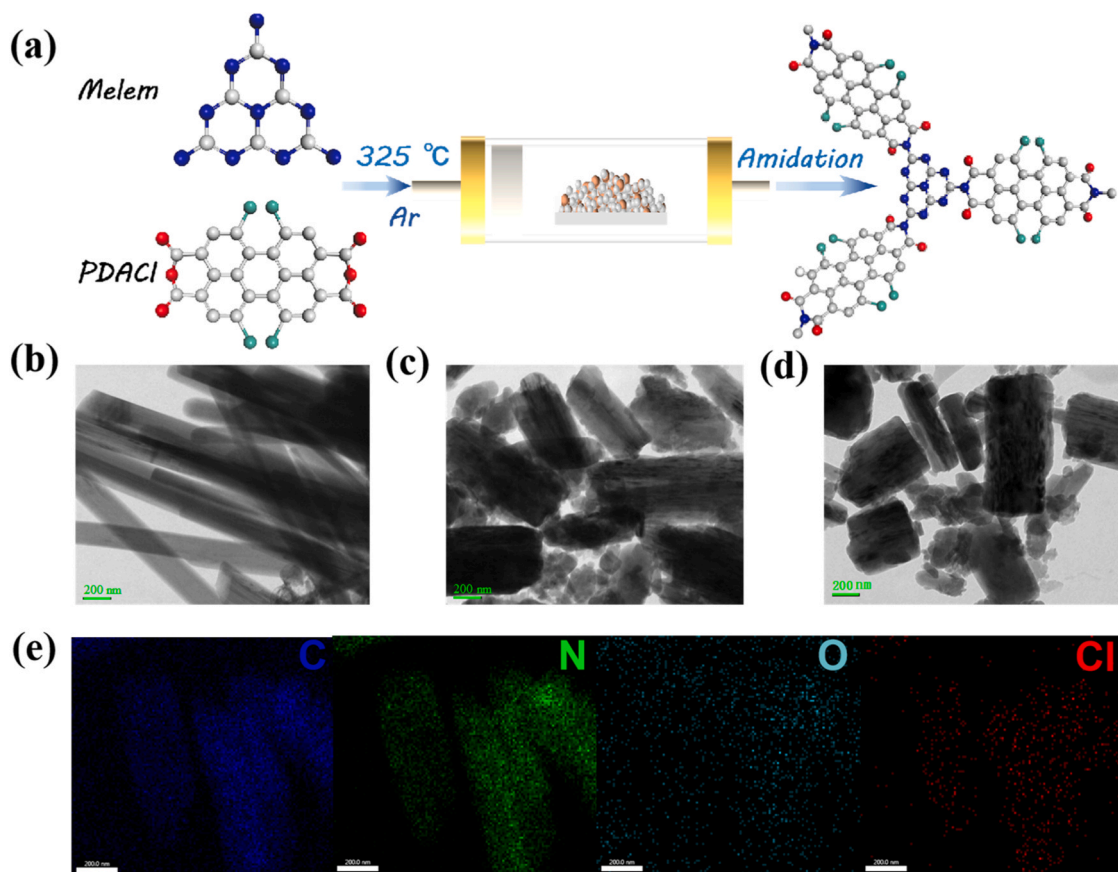


**Fig. 1.** (a) Schematic diagram of the preparation of  $\text{PI}_{\text{Cl}}\text{CN}$ , (b-d) TEM-EDX images of (b) CN, (c) PICN, (d)  $\text{PI}_{\text{Cl}}\text{CN}$ , (e) TEM mapping of  $\text{PI}_{\text{Cl}}\text{CN}$ .

construction is often used to strengthen the built-in electric field. Zhu Yongfa et al. strengthened the built-in electric field by constructing PDI series photocatalytic materials with large molecular dipole moments [31–34]. Li Yuliang et al. also used POSS groups to functionalize both ends of PDI and composite p-CN nanosheets to form a soluble S-type heterogeneous catalyst, which not only improved the photophysical properties of the material, but also enhanced the interface electron transport and photoresponse range [35]. In our previous study, a series of all-organic heterojunctions were constructed by in-situ amidation of PDA with g- $\text{C}_3\text{N}_4$  (or Melem) effectively facilitating the transfer and separation of electron-hole pairs [36–40]. However, previous studies were based on the functionalization of imide group N atom of PDI rather than the functionalization of perylene nucleus. In fact, the functionalization of the perylene nucleus can not only make the molecule display a distorted skeleton, but also increase the electron affinity of PDI. This is mainly because the internal structure of the distorted 3D structure has abundant cavities and open microchannels, which shorten the diffusion length of the photoexcited carriers. It is possible to change the symmetry of the VB and CB orbitals as well, increasing the transition dipole moment, resulting in better charge space separation [41–43]. In addition, by adjusting the introduced electron absorption functional groups (halogens, cyanides, hydroxyl groups, etc.), the band structure of PDI and the intensity of the internal electric field can be regulated.

Based on the above analysis, we utilize Melem and PDA as monomers, and employ thermal polymerization to realize the amidation reaction of PDA and generate the organic heterojunction of Melem and PDI. Simultaneously, the electron-withdrawing substituent -Cl is introduced into the PDI bay position. It is found that the bay -Cl has two effects: (1) it can enhance the electronic tension of perylene ring, thereby strengthening the electric field between Melem and PDI; (2) The steric hindrance effect can be enhanced, causing the molecular structure

of PDI to distort into a quasi-three-dimensional structure, effectively reducing the recombination of electrons and holes. The organic heterojunction exhibits excellent photocatalytic  $\text{H}_2\text{O}_2$  production activity due to the stronger intrinsic electric field and excellent carrier separation effect.

## 2. Results and discussion

### 2.1. Preparation and characterization

Fig. 1a shows the schematic diagram of the synthetic method and the formation process of the  $\text{PI}_{\text{Cl}}\text{CN}$ . Specifically, melem and PDACl were mixed evenly in a mortar. Then, the mixture was introduced into a tubular furnace. Under the argon protection,  $\text{PI}_{\text{Cl}}\text{CN}$  was formed through thermal polymerization at 325 °C. The micromorphology of all samples was characterized by the transmission electron microscopy (TEM). As shown in Fig. 1b, melem exhibited a nanoribbon morphology. The morphology of PICN transformed into short nano-rod, indicating in-situ formation of PICN around the melem nanoribbon. The morphology of  $\text{PI}_{\text{Cl}}\text{CN}$  is similar to that of PICN. Interestingly, the introduction of -Cl into the perylene annulus leads to an increase in the specific surface area of PICN, which may be attributed to the distortion of the molecular structure of PDI into a quasi-three-dimensional structure in the polymer (Figure S1). To confirm the successful introduction of -Cl, the TEM-EDX mapping was performed. As illustrated in Fig. 1e, Cl elements are evenly distributed on the surface of  $\text{PI}_{\text{Cl}}\text{CN}$ .

The chemical structures of CN, PICN and  $\text{PI}_{\text{Cl}}\text{CN}$  were characterized by XRD analysis. The XRD spectrum of CN shows multiple distinct diffraction peaks in the range of  $13.0^\circ \sim 27.4^\circ$  (Figure S2). However, these peaks are different from the XRD peaks of g- $\text{C}_3\text{N}_4$ , indicating this sample is not pure g- $\text{C}_3\text{N}_4$ . According to previous literature, the

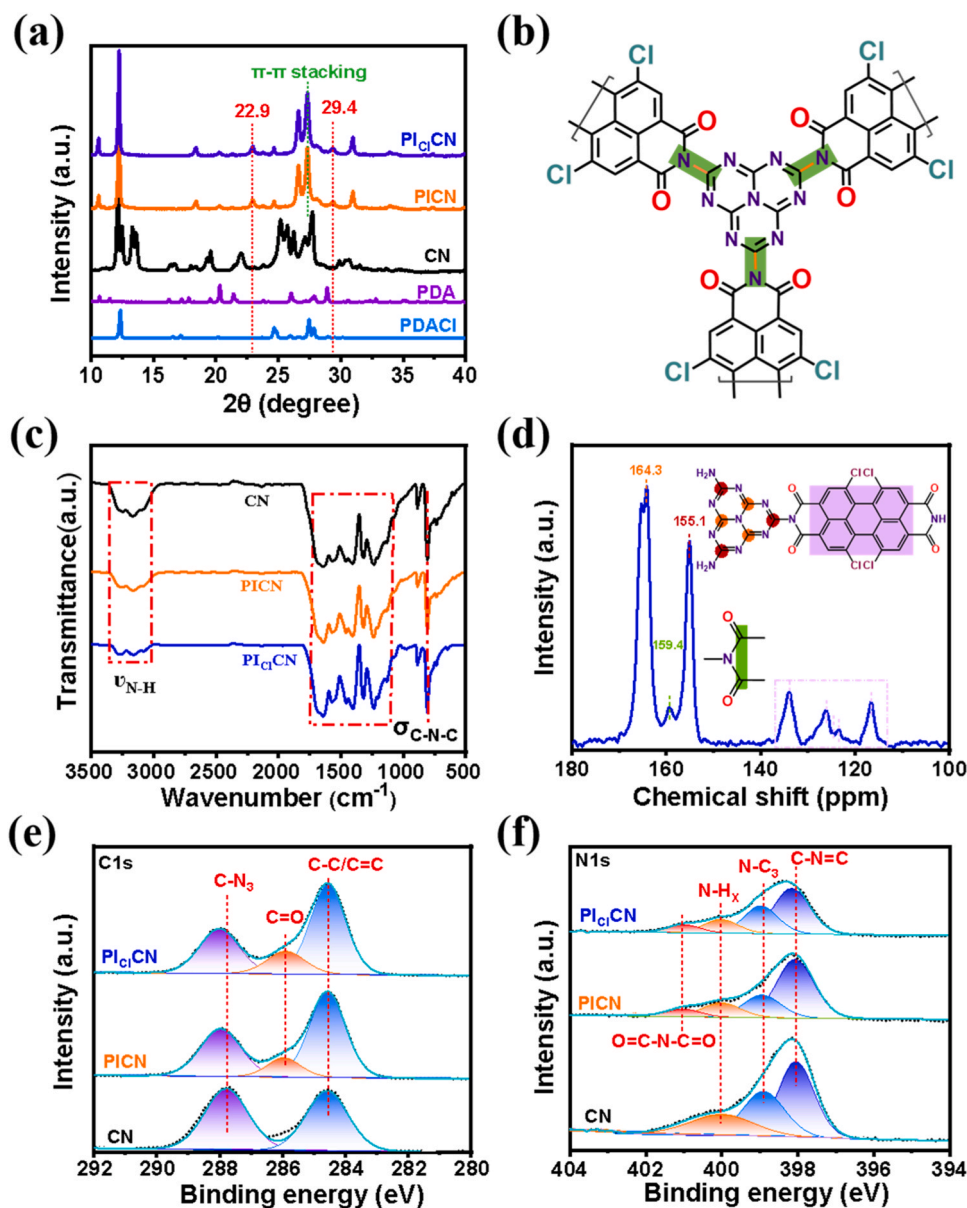


**Fig. 2.** (a) X-ray diffraction patterns of CN, PICN, PI<sub>Cl</sub>CN, PDA and PDACl, (b) Diagram of amide bond in PI<sub>Cl</sub>CN, (c) FT-IR spectra of CN, PICN and PI<sub>Cl</sub>CN, (d) <sup>13</sup>C solid-state NMR spectra of PI<sub>Cl</sub>CN, (e) XPS C1s analysis of CN, PICN and PI<sub>Cl</sub>CN, (f) XPS N1s analysis of CN, PICN and PI<sub>Cl</sub>CN.

diffraction peaks of this sample are consistent with the XRD diffraction peaks of Melem. Compared with the XRD diffraction of CN, PDA and PDACl, XRD patterns of PICN and PI<sub>Cl</sub>CN show obvious diffraction peaks at 22.2° and 29.4°, which may be attributed to the successful amidation of PDA and PDACl with CN. Notably, the  $\pi$ - $\pi$  stacking structure of PICN and PI<sub>Cl</sub>CN occurs at 27.4°, which is consistent with previous literatures [32,44] (Fig. 2a and b). FT-IR spectra further confirmed the amidation reaction, as shown in Fig. 2c, the peak at 808 cm<sup>-1</sup> can be attributed to the out-of-plane bending vibrational properties of the triazine ring, and the peaks in the range of 1200 ~ 1740 cm<sup>-1</sup> refer to the typical stretching vibrational modes of N=C-N heterocycles. Multiple broad peaks located in the region of 3000 ~ 3300 cm<sup>-1</sup> can be attributed to the stretching vibrational absorption peaks of -NH<sub>2</sub> [38]. Compared with CN, the absorption peaks of -NH<sub>2</sub> in PICN and PI<sub>Cl</sub>CN are obviously weakened. Meanwhile, the characteristic peaks of anhydride group in the FT-IR spectra of PDA and PDACl disappear in the FT-IR spectra of PICN and PI<sub>Cl</sub>CN (Figure S3 and S4). These phenomena indicate that anhydride groups of PDA and PDACl have reacted with -NH<sub>2</sub> groups of Melem through the amidation reaction. The structure of PI<sub>Cl</sub>CN was

further confirmed by solid-state <sup>13</sup>C NMR spectra. As depicted in Fig. 2d, the carbon atoms in the PDICl moiety on the conjugated ring exhibit peaks at 133.9, 126.3, 124.6, 123.3, and 116.5 ppm, the specific attribution of C atom was illustrated in Figure S5 [45]. The carbonyl carbon in the PDICl moiety appears at a high chemical shift of 159.4 ppm, while the peaks at 164.3 and 155.1 ppm are attributed to the carbon atoms in the CN group (as shown in Figure S6).

In addition to the above characterizations, high resolution XPS spectra of C 1s and N 1s further confirm the formation of amide bonds. The C1s high-resolution spectrum of CN can be divided into two peaks at the binding energy of 284.6 eV and 287.7 eV (Fig. 2e). The peak at 287.7 eV is caused by the sp<sup>2</sup> hybridized C atom in the triazine ring, while the peak at 284.6 eV is almost certainly caused by the C-C group in the ambient atmosphere. For PICN and PI<sub>Cl</sub>CN, both peaks still exist, but the peak at 284.6 eV is stronger than that of CN. The strengthening of the C-C group is likely due to the presence of C in the perylene ring, indicating the successful synthesis of PDI and PDICl [40]. A new distinct peak at 285.9 eV further supports this conclusion, corresponding to the -C=O group in the PICN or PI<sub>Cl</sub>CN structure. The N1s high resolution

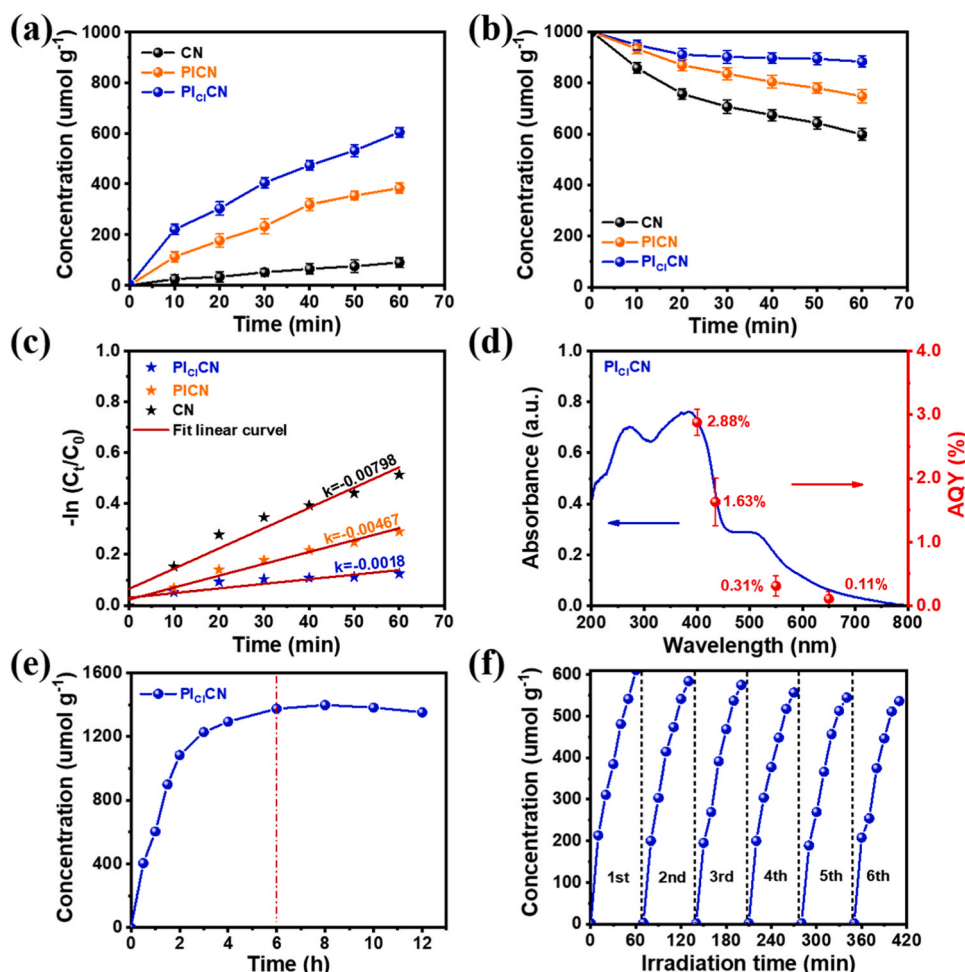


**Fig. 3.** (a) Time-dependent photocatalysis of H<sub>2</sub>O<sub>2</sub> synthesis by CN, PICN, PI<sub>Cl</sub>CN, (b) Photocatalytic decomposition behavior of H<sub>2</sub>O<sub>2</sub> under visible light irradiation and argon atmosphere, (c) First order kinetics of decomposition of CN, PICN, PI<sub>Cl</sub>CN, (d) Apparent quantum yield of PI<sub>Cl</sub>CN, (e) Photocatalytic stability production of H<sub>2</sub>O<sub>2</sub> in continuous PI<sub>Cl</sub>CN reaction for 12 h, (f) Cyclic stability test of PI<sub>Cl</sub>CN photocatalytic generation of H<sub>2</sub>O<sub>2</sub>.

spectrum of CN exhibits three peaks at 398.0, 398.9, 400.0 eV, corresponding to sp<sup>2</sup> hybrid N atom, bridging N atom and amino N atom, respectively (Fig. 2f). These three peaks are also present in the N1s spectra of PICN and PI<sub>Cl</sub>CN, but the peak position of sp<sup>2</sup> hybrid N atoms in PICN and PI<sub>Cl</sub>CN has shifted approximately 0.1 eV towards higher energy. This shift shows a reduction in the electron density of sp<sup>2</sup> hybrid N atoms. Moreover, a new peak appears at 401.0 eV in the N1s high-resolution spectra of PICN and PI<sub>Cl</sub>CN. This new peak can be attributed to the N atom of O=C-N-C=O, providing strong evidence for the formation of PDI and PDICl. Due to the strong electron absorption ability of Cl atoms, the electron density of sp<sup>2</sup> hybrid N atom decreases after the formation of PI<sub>Cl</sub>CN.

## 2.2. Photocatalytic H<sub>2</sub>O<sub>2</sub> production activity

The visible-light-induced photocatalytic performance of produced photocatalysts was evaluated by the H<sub>2</sub>O<sub>2</sub> generation without the need of any sacrificial reagent (Fig. 3a and S7). After visible light irradiation for 60 mins, CN exhibits minimal H<sub>2</sub>O<sub>2</sub> generation performance (90.7  $\mu\text{mol g}^{-1}\text{h}^{-1}$ ) among different samples. After the PDI grafting, the H<sub>2</sub>O<sub>2</sub> yield of PICN (382.7  $\mu\text{mol g}^{-1}\text{h}^{-1}$ ) is 4.2 times higher than that of CN. After the introduction of -Cl groups at the bay positions of PDI, the H<sub>2</sub>O<sub>2</sub> production of PI<sub>Cl</sub>CN is further increased about 1.6 times (604.2  $\mu\text{mol g}^{-1}\text{h}^{-1}$ ) compared to that of PICN. The comparison of H<sub>2</sub>O<sub>2</sub> production properties of similar materials is shown in Table S1. The excellent H<sub>2</sub>O<sub>2</sub> production activity of PI<sub>Cl</sub>CN is attributed to the strong electric field, the

low O<sub>2</sub> adsorption energy, and the small overpotential of O<sub>2</sub> reduction reaction. However, with the extension of the reaction time, the H<sub>2</sub>O<sub>2</sub> production rate of PI<sub>Cl</sub>CN gradually tends to the equilibrium, which may be caused by the simultaneous production and decomposition of H<sub>2</sub>O<sub>2</sub>. Therefore, H<sub>2</sub>O<sub>2</sub> decomposition experiments were conducted for all samples (Fig. 3b). Among different samples, H<sub>2</sub>O<sub>2</sub> exhibits the slowest decomposition rate on PI<sub>Cl</sub>CN. When the light irradiation exceeds 30 mins, the decomposition rate of H<sub>2</sub>O<sub>2</sub> becomes very slow. According to the decomposition rate constant of H<sub>2</sub>O<sub>2</sub>, the PI<sub>Cl</sub>CN exhibited excellent stability, as shown in Fig. 3c. The decomposition rate constants of H<sub>2</sub>O<sub>2</sub> over CN and PICN are  $-0.00798$  and  $-0.00467$ , which are 4.4 times and 2.6 times of that over PI<sub>Cl</sub>CN ( $-0.0018$ ), respectively. This phenomenon indicates that the introduction of chlorine contributes to the accumulation of H<sub>2</sub>O<sub>2</sub> which may be attributed to the fact that the active sites on PI<sub>Cl</sub>CN are dominated by O<sub>2</sub> adsorption, and the produced H<sub>2</sub>O<sub>2</sub> molecules are protected.

To evaluate the light energy utilization efficiency of PI<sub>Cl</sub>CN during the process of H<sub>2</sub>O<sub>2</sub> generation, the apparent quantum yield (AQY) under the monochromatic light irradiation was measured (Fig. 3d). The AQY at 400, 435, 550 and 650 nm were 2.88%, 1.63%, 0.31% and 0.11%, respectively. However, the AQY of PICN and CN at 400 nm was only 1.78% and 0.5%, respectively (Figure S8 and S9). To further verify the activity stability of PI<sub>Cl</sub>CN, the continuous experiment and cyclic test for H<sub>2</sub>O<sub>2</sub> generation on PI<sub>Cl</sub>CN was carried out, respectively (Fig. 3e and f). After 6 cycles under visible light irradiation for a total of 6 h, no obvious decrease in photocatalytic H<sub>2</sub>O<sub>2</sub> production can be observed,



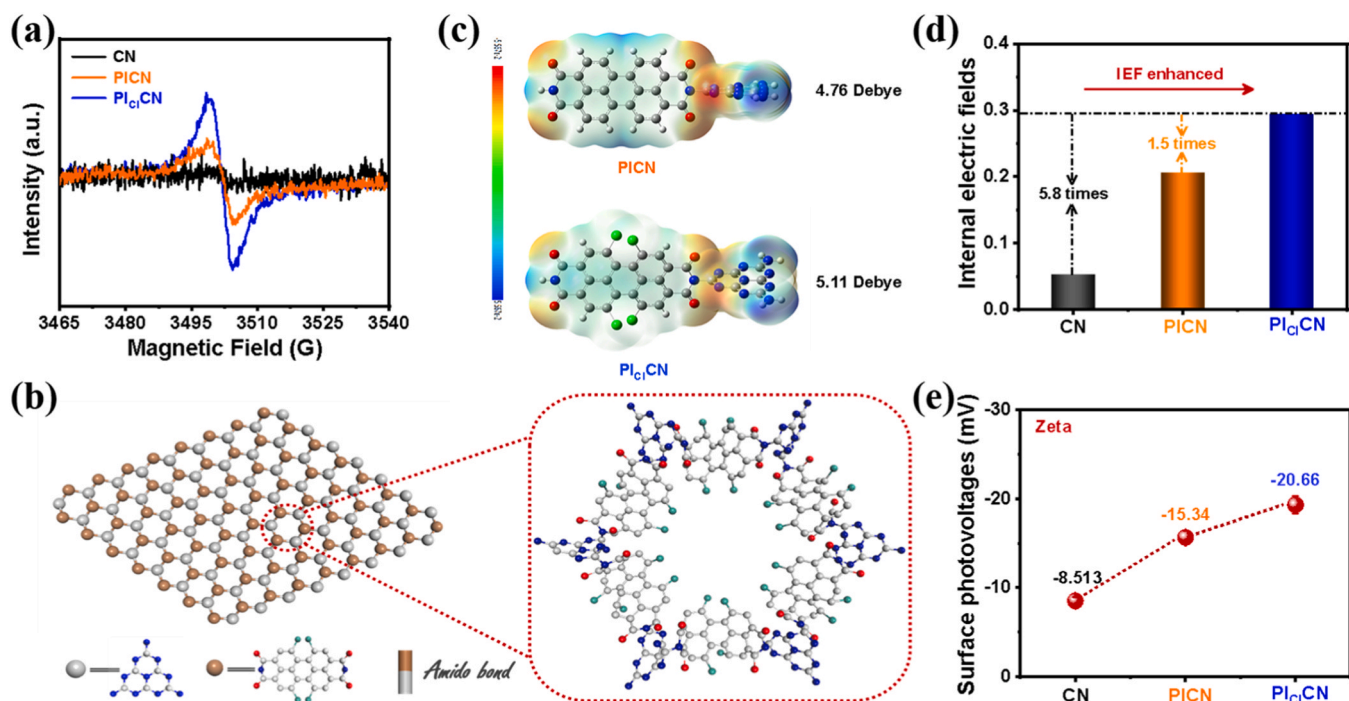


**Fig. 4.** (a) EPR spectra of CN, PICN and PI<sub>Cl</sub>CN, (b) Schematic diagram of PI<sub>Cl</sub>CN (c) ESP distribution of optimized PICN and PI<sub>Cl</sub>CN model, (d) corresponding IEF intensity comparison of different samples, (e) Zeta average potential.

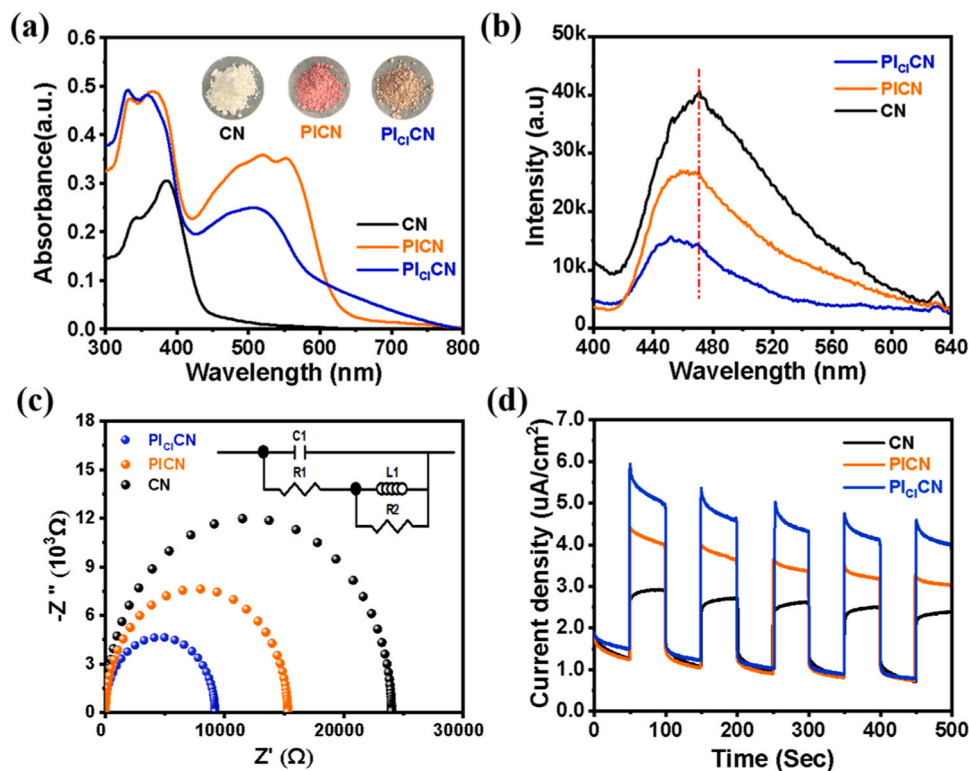


**Fig. 5.** (a) UV-vis spectra of CN, PICN and PI<sub>Cl</sub>CN, (b) PL spectroscopy of CN, PICN and PI<sub>Cl</sub>CN, (c) EIS spectra of CN, PICN and PI<sub>Cl</sub>CN, (d) Transient.

indicating the excellent stability of PI<sub>Cl</sub>CN activity under the visible light irradiation.

### 2.3. Photocatalytic mechanism

Since PDI and PDICl have strong electron-withdrawing groups

(-C=O and -Cl), the introduced PDI and PDICl may form the electron donor-acceptor relationship with CN, thereby influencing the electron dissociation of CN. As shown in Fig. 4a, the EPR signals of both PICN and PI<sub>Cl</sub>CN are stronger than that of CN. Moreover, the introduction of -Cl further enhances this delocalization effect (Fig. 4b). It is well known that there is usually an electric field between the electron donor and the

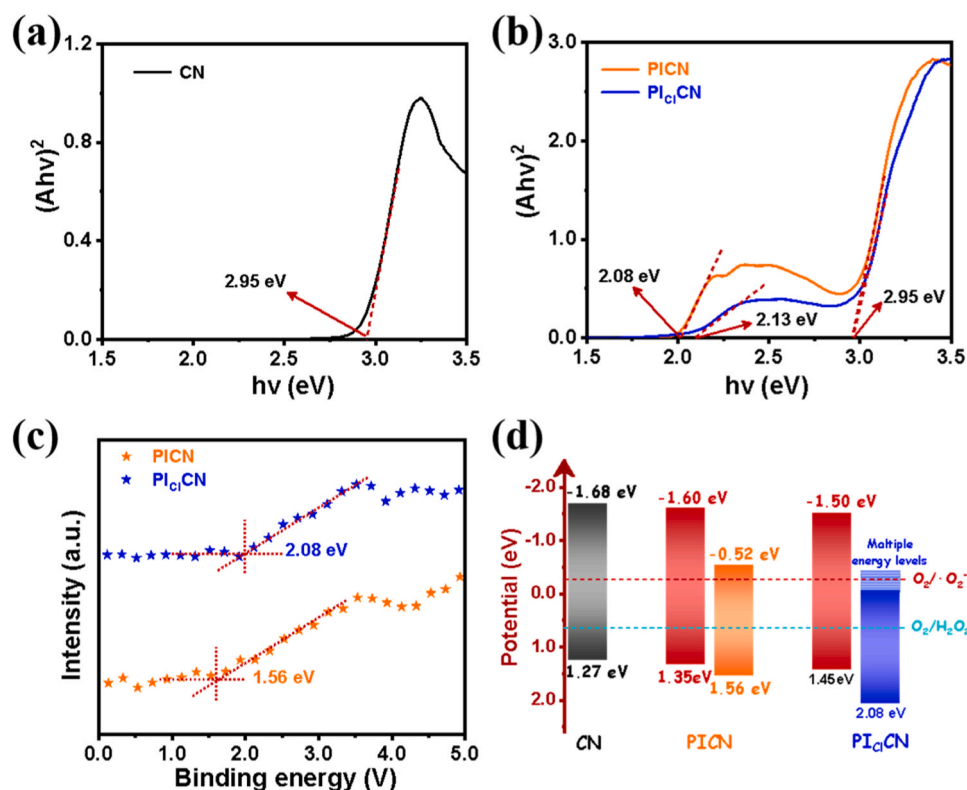


Fig. 6. Band gap images of CN(a), PICN and PI<sub>Cl</sub>CN (b), (c) Valence band of PICN and PI<sub>Cl</sub>CN, (d) Schematic diagram of the positions of the energy bands.

acceptor. The interfacial electric field is conducive to the separation of photogenerated carrier, and thus improves the photocatalytic performance of the photocatalyst. The intensity of the electric field within the molecule can be determined by the value of molecular dipole[34,46,47]. The larger the molecular dipole, the stronger the electric field. To get the molecular dipole value of different samples, the surface electrostatic potential distributions were simulated through computer. As shown in Fig. 4c, the introduction of Cl atoms results in the PDI portion absorbing more negative charges. Meanwhile, Cl atoms increase the molecular dipole value of PICN from 4.76D to 5.11D, confirming Cl atoms could improve the interfacial electric fields between PDI and CN. The internal electric field (IEF) strength of all samples is calculated according to the formula of IEF proposed by Kanata theory[48] (the detailed process is in the supporting information S5, Figure S10). As shown in Fig. 4d, The IEF of PI<sub>Cl</sub>CN is 1.5 times and 5.8 times of PICN and CN, respectively. Simultaneously, the electronegativity is enhanced due to the formation of all-organic heterojunctions in PICN, which is further enhanced by the introduction of -Cl, as shown in Fig. 4e and Table S2.

The introduction of PDI and PDICl significantly influences the optical and electrical properties of CN, as depicted and compared in Fig. 5. Fig. 5a shows the UV-vis diffuse reflectance spectra (DRS) of all the samples. Relative to CN, the introduction of PDI and PDICl obviously alters the light absorption range of CN. CN can only absorb light below 500 nm. However, PICN exhibits two additional absorption bands in the range of 500–600 nm, which is a typical PDI characteristic absorption. After grafting of -Cl functional group at the bay site of PDI, the light absorption range of PI<sub>Cl</sub>CN further extends to 800 nm. This could be attributed to the heavy atom effect, introducing multiple energy levels below the conduction band[49].

Generally, the electron donor-acceptor relationship and the interfacial electric field could facilitate the separation of photo-generated carriers. To further investigate the separation efficiency of the photo-generated carriers, fluorescence emission spectra (PL) were measured. As shown in Fig. 5b and S11, CN has a strong PL emission peak at

471 nm. The introduction of PDI could reduce the intensity of PL emission peak of CN, and the introduction of -Cl groups could further reduce the PL emission peak of PICN. Accordingly, PI<sub>Cl</sub>CN exhibited the lowest PL intensity and longer lifetime of charge carriers, this phenomenon confirms that the electron donor-acceptor relationship and the interfacial electric field could facilitate the transfer of photo-generated carriers. This can be further proved by the electrochemical impedance spectroscopy (EIS). As shown in Fig. 5c, the introduction of PDI reduces the impedance of CN, and the introduction of -Cl further reduces the impedance of PICN. The smaller impedance can produce more photo-generated electrons for photocatalytic reactions. This can be proved by the results of transient photocurrent. As shown in Fig. 5d, PICN shows a higher photocurrent than CN, and PI<sub>Cl</sub>CN shows the highest photocurrent among the three samples.

Usually small molecules (such as Melem, PDA and PDACl) may have discrete energy level structures. However, when these molecules aggregate, their energy levels will split to form the band structures[50, 51]. In addition, the production of long-lived excitons in polymer semiconductor photocatalysts through the regulation of heavy atom effects can comprehensively improve the efficiency of photocatalysis [52]. Therefore, it is necessary to analyze the band structure of the polymer, and it can be observed from the Tauc plot that the band gap energy ( $E_g$ ) of CN is 2.95 eV (Fig. 6a). However, PICN and PI<sub>Cl</sub>CN have two bandgap energies, corresponding to the CN portion and PDI (PDICl) portion, respectively. As can be seen from the Fig. 6b, the bandgap energies of PDI and PDICl are 2.08 eV and 2.13 eV, respectively. Compared with PDI, the band gap energy of PDICl increases by 0.05 eV due to the molecular structural distortion caused by the large atomic radius of Cl atoms. The distorted molecular structure cannot effectively promote spin-orbit coupling (SOC) to reduce the energy band difference of PDICl [53]. To further clarify the band structure of all samples, XPS-VB spectroscopy was used to determine the valence band potential of PDI and PDICl in the composite material as 1.56 eV and 2.08 eV, respectively (Fig. 6c), and the price band of pure CN was 1.27 eV (Figure S12d).

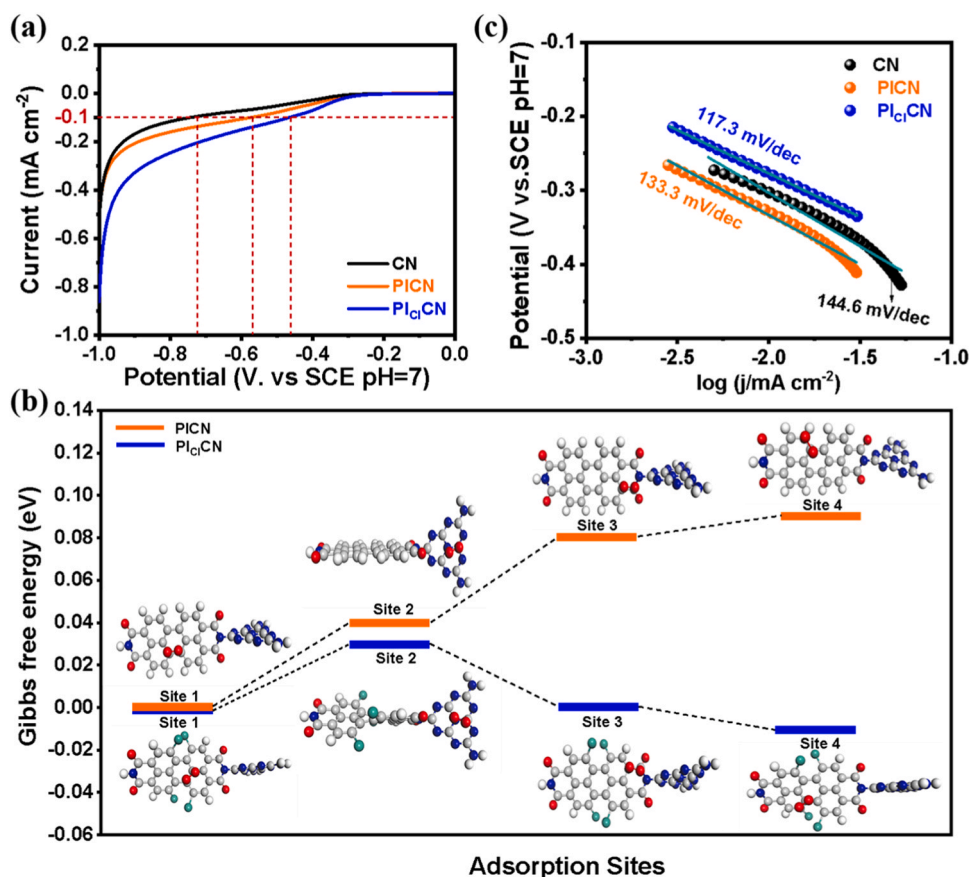


**Fig. 7.** (a) LSV curves of CN, PICN and PI<sub>Cl</sub>CN, (b) Calculated Gibbs free energy diagram of oxygen adsorption on different active sites in PICN and PI<sub>Cl</sub>CN, (c) Tafel slopes of CN, PICN and PI<sub>Cl</sub>CN.

Combined the results of the Mott-Schottky plot, the band structures of all samples can be depicted. (Figure S12a-c, in supplementary materials). As shown in Fig. 6d, the staggered band structure of CN, PDI, and PDICl provides conditions for the construction of stable type II heterojunctions (PICN and PI<sub>Cl</sub>CN). This is consistent with previous reports [34]. Importantly, the heavy atom effect can regulate the excited state band structure of the molecule, resulting in the formation of a multi-level structure under the PDICl conduction band. Compared with PDI, the multi-level structure of PDICl is conducive to the charge transfer at the interface of PDICl and CN, allowing more electrons participate in the O<sub>2</sub> reduction reaction, then promoting the formation of H<sub>2</sub>O<sub>2</sub>.

To investigate whether there is interfacial electron transport between melem and PDI or PDICl, we constructed the interfacial sub-structure model of PICN (Figure S13) and PI<sub>Cl</sub>CN (Figure S14). As shown in Figure S15, DFT theoretical calculation results suggest that the charge transfer at PICN interfaces mainly occurs from melem to PDI with a required minimum energy of 3.0 eV. When Cl atom is introduced into the bay position of PDI part, the direction of interfacial charge transport remains unchanged. However, the minimum energy required for electrons to transfer from melem to PDI is reduced by 0.32 eV, indicating that the introduction of bay -Cl can promote electron transport at the interface between CN and PDI.

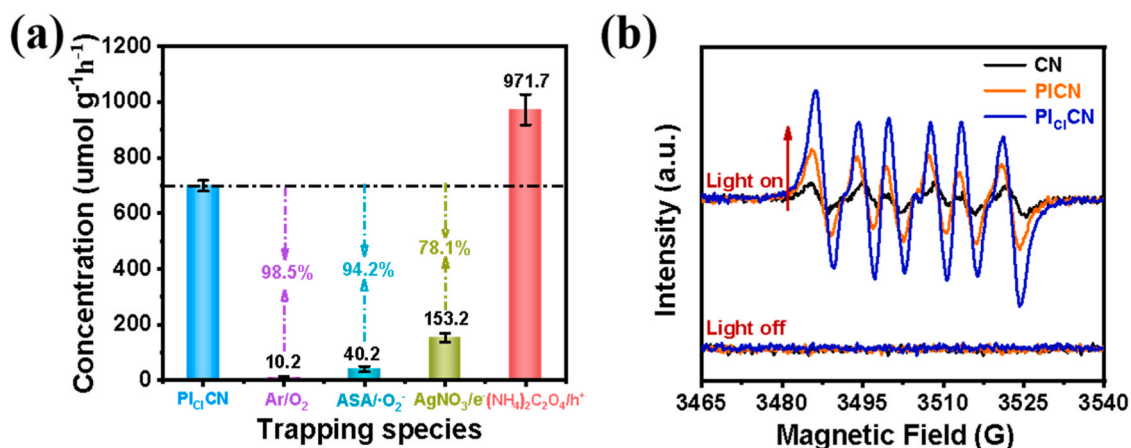


**Fig. 8.** (a) The effect of different trapping reagents on photocatalytic production of H<sub>2</sub>O<sub>2</sub> from PI<sub>Cl</sub>CN under the same photocatalytic conditions (b) EPR spectra of the DMPO-O<sub>2</sub> adduct for CN, PICN, PI<sub>Cl</sub>CN.

The photocatalytic activity is not only related to the quantity of photogenerated electrons but also to the overpotential of the reaction on the material surface. The lower overpotential contributes to the higher catalytic activity. To get the overpotential values of oxygen reduction reaction (ORR) over different samples, linear sweep voltammetry (LSV) was performed in an O<sub>2</sub>-saturated Na<sub>2</sub>SO<sub>4</sub> (0.1 M) electrolyte solution. As shown in Fig. 7a, when the current density is 0.1 mA cm<sup>-2</sup>, PI<sub>Cl</sub>CN has a small overpotential of 461 mV. In contrast, the ORR activity of in-situ grafted PDI nanosheets on CN was lower (567 mV, j=0.1 mA cm<sup>-2</sup>). As is well known, the overpotential of the ORR reaction is always affected by the O<sub>2</sub> adsorption and activation. Therefore, the adsorption position and adsorption energy of O<sub>2</sub> over PICN and PI<sub>Cl</sub>CN surfaces were simulated by DFT theory, as illustrated in Fig. 7b.

According to the molecular structure of the material, there are 4 adsorption sites where O<sub>2</sub> is presented on PICN. The computational results show that only site 1 has O<sub>2</sub> adsorption energy less than 0 eV, while the O<sub>2</sub> adsorption energies at the other three sites are greater than 0 eV. This indicates that O<sub>2</sub> can only be adsorbed at site 1. Upon the introduction of Cl atoms at the PDI bay site, the adsorption energies of O<sub>2</sub> at all four adsorption sites decrease. At the same time, the adsorption energies of O<sub>2</sub> at sites 1, 3, and 4 is less than or equal to 0 eV, indicating that the adsorption of O<sub>2</sub> at these sites can occur spontaneously. The introduction of Cl atoms at PDI bay site can not only reduce the overpotential of O<sub>2</sub> reduction reaction, but also increase the adsorption site and adsorption capacity of O<sub>2</sub>, improving the efficiency of O<sub>2</sub> reduction reaction.

Generally, the value of Tafel slope reflects the kinetic characteristics of the reaction. A smaller Tafel slope may reflect a smaller reaction overpotential and faster reaction kinetics. As shown in Fig. 7c, the Tafel slope of PI<sub>Cl</sub>CN is 117.3 mV/dec by fitting LSV curve, which is much lower than that of CN (144.6 mV/dec) and PICN (133.3 mV/dec), confirming the presence of Cl atoms enhances the ORR kinetic process of PI<sub>Cl</sub>CN.

To gain a deeper insight into the mechanism of photocatalytic H<sub>2</sub>O<sub>2</sub> evolution on PI<sub>Cl</sub>CN, a series of active species capture experiments were conducted using various scavengers. Ascorbic acid (ASA), (NH<sub>4</sub>)<sub>2</sub>C<sub>2</sub>O<sub>4</sub> and AgNO<sub>3</sub> were employed to capture superoxide radical ( $\cdot\text{O}_2^-$ ), hole (h<sup>+</sup>) and electron (e<sup>-</sup>), respectively. Fig. 8a demonstrates a significant decrease in H<sub>2</sub>O<sub>2</sub> production when an anaerobic environment was created by introducing Ar gas into the reaction system instead of O<sub>2</sub>. This result indicates the necessity of O<sub>2</sub> for H<sub>2</sub>O<sub>2</sub> production. The addition of AgNO<sub>3</sub> lead to a rapid decline in H<sub>2</sub>O<sub>2</sub> yield, implying that the formation of H<sub>2</sub>O<sub>2</sub> occurred via the reduction of O<sub>2</sub> by electrons. Notably, the addition of ASA results in a significant reduction in H<sub>2</sub>O<sub>2</sub> production, indicating that  $\cdot\text{O}_2^-$  serves as a crucial intermediate in H<sub>2</sub>O<sub>2</sub> production (through the consecutive reactions: O<sub>2</sub> + e<sup>-</sup> →  $\cdot\text{O}_2^-$  and  $\cdot\text{O}_2^- + 2\text{H}^+ + \text{e}^- \rightarrow \text{H}_2\text{O}_2$ ). In contrast, the addition of (NH<sub>4</sub>)<sub>2</sub>C<sub>2</sub>O<sub>4</sub>, which can capture h<sup>+</sup>, indirectly enhances the separation efficiency of electrons and holes, leading to more electrons participating in H<sub>2</sub>O<sub>2</sub> generation and thus an increase in H<sub>2</sub>O<sub>2</sub> production.

To provide convincing evidence, the presence of  $\cdot\text{O}_2^-$  was further confirmed by 5, 5-dimethyl-1-pyrroline N-oxide (DMPO) EPR capture experiments. As shown in Fig. 8b, the superoxide trapping agent DMPO does not exhibit the typical signal peak of DMPO- $\cdot\text{O}_2^-$  in any samples under dark conditions, but after 3 mins of illumination, typical DMPO- $\cdot\text{O}_2^-$  signals were recorded, with the signal intensities in the order of PI<sub>Cl</sub>CN > PICN > CN. This is the key factor for PI<sub>Cl</sub>CN to produce more H<sub>2</sub>O<sub>2</sub> under visible light irradiation conditions.

### 3. Conclusion

In summary, we successfully constructed an all-organic heterojunction PICN using CN and PDA. Compared with the intrinsic CN, the abundant heterojunction structure of PICN forms a large and uniform conjugated plane. The introduction of -Cl at the bay position of PDI enhanced the interfacial electric in PI<sub>Cl</sub>CN, accelerating the separation

efficiency of electron-hole pairs. Additionally, the introduction of -Cl at PDI bay enhances the electron delocalization effect as well, reducing the energy required for electron transport from Melem to PDICl, and promoting the interfacial electron transport of PI<sub>Cl</sub>CN under visible light irradiation. In the absence of any precious metals and sacrificial, PI<sub>Cl</sub>CN achieves efficient photocatalytic production of hydrogen peroxide under visible light, with a H<sub>2</sub>O<sub>2</sub> yield of 604.2 μmol g<sup>-1</sup> h<sup>-1</sup>, which is 1.6 times higher than that of PICN. At the same time, PI<sub>Cl</sub>CN exhibits a high apparent quantum yield (AQY) of 2.88% at 400 nm. This study provides a new idea for the construction of all organic heterojunctions and the design of interfacial electric field tuning.

### CRediT authorship contribution statement

**Kajsa Uvdal:** Formal analysis, Software. **Tingting Dong:** Writing – review & editing, Writing – original draft, Software, Investigation, Data curation. **Guohui Dong:** Writing – review & editing, Supervision, Resources. **Kai Han:** Writing – original draft, Investigation. **Caihong Chen:** Writing – original draft, Software. **Jiwen Hu:** Writing – review & editing, Supervision.

### Declaration of Competing Interest

The authors declare that they have no known competing financial interests or personal relationships that could have appeared to influence the work reported in this paper.

### Data availability

Data will be made available on request.

### Acknowledgment

Financial support by the National Natural Science Foundation of China (Grant No. 21876104) is gratefully acknowledged. Supported by the National Foreign experts project high-end foreign experts introduction plan (G2022041003). Supported by the Open Project Program of the State Key Laboratory of Photocatalysis on Energy and Environment (Grant No. SKLPEE-KF 202312), Fuzhou University. Supported by the Swedish Government Strategic Research Area in Materials Science on Functional Materials at Linköping University (Faculty Grant SFO-Mat-LiU No. 2009-00971).

### Supporting information

The Supporting Information is available free of charge on the Elsevier Publications website.

Additional experimental details, materials, methods, BET measurements, FT-IR, XRD, <sup>13</sup>C NMR, PL measurements, apparent quantum yield (AQY), Hydrogen peroxide activity test, internal electric field (IEF) and energy band calculations, Zeta potential, transient PL spectra, Mott-schottky (MS) plots, theoretical calculations.(PDF)

### Appendix A. Supporting information

Supplementary data associated with this article can be found in the online version at doi:10.1016/j.apcatb.2024.124144.

### References

- [1] T. Liu, Z. Pan, J.J.M. Vequizo, K. Kato, B. Wu, A. Yamakata, K. Katayama, B. Chen, C. Chu, K. Domen, Overall photosynthesis of H<sub>2</sub>O<sub>2</sub> by an inorganic semiconductor, Nat. Commun. 13 (2022) 1034, <https://doi.org/10.1038/s41467-022-28686-x>.
- [2] X. Cao, A. Huang, C. Liang, H.C. Chen, T. Han, R. Lin, Q. Peng, Z. Zhuang, R. Shen, H.M. Chen, Y. Yu, C. Chen, Y. Li, Engineering lattice disorder on a photocatalyst: photochromic BiOBr nanosheets enhance activation of aromatic C-H bonds via



- water oxidation, *J. Am. Chem. Soc.* 144 (2022) 3386–3397, <https://doi.org/10.1021/jacs.1c10112>.
- [3] X. Zhang, P. Ma, C. Wang, L. Gan, X. Chen, P. Zhang, Y. Wang, H. Li, L. Wang, X. Zhou, Unraveling the dual defect sites in graphite carbon nitride for ultra-high photocatalytic H<sub>2</sub>O<sub>2</sub> evolution, *Energy Environ. Sci.* 15 (2022) 830–842, <https://doi.org/10.1039/D1EE02369A>.
  - [4] S. Wang, Z. Xie, D. Zhu, S. Fu, Y. Wu, H. Yu, C. Lu, P. Zhou, M. Bonn, H.I. Wang, Q. Liao, H. Xu, X. Chen, C. Gu, Efficient photocatalytic production of hydrogen peroxide using dispersible and photoactive porous polymers, *Nat. Commun.* 14 (2023) 6891, <https://doi.org/10.1038/s41467-023-42720-6>.
  - [5] H. Luo, T. Shan, J. Zhou, L. Huang, L. Chen, R. Sa, Y. Yamauchi, J. You, Y. Asakura, Z. Yuan, H. Xiao, Controlled synthesis of hollow carbon ring incorporated g-C<sub>3</sub>N<sub>4</sub> tubes for boosting photocatalytic H<sub>2</sub>O<sub>2</sub> production, *Appl. Catal. B: Environ.* 337 (2023) 122933, <https://doi.org/10.1016/j.apcatb.2023.122933>.
  - [6] Q. Wu, J. Cao, X. Wang, Y. Liu, Y. Zhao, H. Wang, Y. Liu, H. Huang, F. Liao, M. Shao, A metal-free photocatalyst for highly efficient hydrogen peroxide photoproduction in real seawater, *Nat. Commun.* 12 (2021) 483, <https://doi.org/10.1038/s41467-020-20823-8>.
  - [7] C. Zhang, W. Shen, K. Guo, M. Xiong, J. Zhang, X. Lu, A pentagonal defect-rich metal-free carbon electrocatalyst for boosting acidic O<sub>2</sub> reduction to H<sub>2</sub>O<sub>2</sub> production, *J. Am. Chem. Soc.* 145 (2023) 11589–11598, <https://doi.org/10.1021/jacs.3c00689>.
  - [8] Z. Wu, P. Ding, V. Gueskine, R. Boyd, E.D. Glowacki, M. Odén, X. Crispin, M. Berggren, E.M. Björk, M. Vagin, Conducting polymer-based e-refinery for sustainable hydrogen peroxide production, *Energy Environ. Mater.* 0 (2023) e12551, <https://doi.org/10.1002/eem.12551>.
  - [9] C. Wang, T.Y. Qiu, Y.N. Zhao, Z.L. Lang, Y.G. Li, Z.M. Su, H.Q. Tan, Phosphorus-alkynyl functionalized covalent triazine/heptazine-based frameworks for high-performance photocatalytic hydrogen peroxide production, *Adv. Energy Mater.* 13 (2023) 2301634, <https://doi.org/10.1002/aenm.202301634>.
  - [10] E. Jung, H. Shin, B.H. Lee, V. Efremov, S. Lee, H.S. Lee, J. Kim, W. Hooch Antink, S. Park, K.S. Lee, S.P. Cho, J.S. Yoo, Y.E. Sung, T. Hyeon, Atomic-level tuning of Co-N-C catalyst for high-performance electrochemical H<sub>2</sub>O<sub>2</sub> production, *Nat. Mater.* 19 (2020) 436–442, <https://doi.org/10.1038/s41563-019-0571-5>.
  - [11] S. Wang, B. Cai, H. Tian, Efficient generation of hydrogen peroxide and formate by an organic polymer dots photocatalyst in alkaline conditions, *Angew. Chem. Int. Ed.* 61 (2022) e202202733, <https://doi.org/10.1002/anie.202202733>.
  - [12] W. Zhao, P. Yan, B. Li, M. Bahri, L. Liu, X. Zhou, R. Clowes, N.D. Browning, Y. Wu, J.W. Ward, A.I. Cooper, Accelerated synthesis and discovery of covalent organic framework photocatalysts for hydrogen peroxide production, *J. Am. Chem. Soc.* 144 (2022) 9902–9909, <https://doi.org/10.1021/jacs.2c02666>.
  - [13] H. Peng, H. Yang, J. Han, X. Liu, D. Su, T. Yang, S. Liu, C.W. Pao, Z. Hu, Q. Zhang, Y. Xu, H. Geng, X. Huang, Defective ZnIn<sub>2</sub>S<sub>4</sub> nanosheets for visible-light and sacrificial-agent-free H<sub>2</sub>O<sub>2</sub> photosynthesis via O<sub>2</sub>/H<sub>2</sub>O redox, *J. Am. Chem. Soc.* 145 (2023) 27757–27766, <https://doi.org/10.1021/jacs.3c10390>.
  - [14] S. Qu, H. Wu, Y.H. Ng, Clean production of hydrogen peroxide: a heterogeneous solar-driven redox process, *Adv. Energy Mater.* 13 (2023) 2301047, <https://doi.org/10.1002/aenm.202301047>.
  - [15] K. Kim, J. Park, H. Kim, G.Y. Jung, M.-G. Kim, Solid-phase photocatalysts: physical vapor deposition of Au nanoislands on porous TiO<sub>2</sub> films for millimolar H<sub>2</sub>O<sub>2</sub> production within a few minutes, *ACS Catal.* 9 (2019) 9206–9211, <https://doi.org/10.1021/acscatal.9b02269>.
  - [16] L. Zheng, J. Zhang, Y.H. Hu, M. Long, Enhanced photocatalytic production of H<sub>2</sub>O<sub>2</sub> by nafion coatings on S,N-codoped graphene-quantum-dots-modified TiO<sub>2</sub>, *J. Phys. Chem. C* 123 (2019) 13693–13701, <https://doi.org/10.1021/acs.jpcc.9b02311>.
  - [17] Y. Wu, Y. Yang, M. Gu, C. Bie, H. Tan, B. Cheng, J. Xu, 1D/0D heterostructured ZnIn<sub>2</sub>S<sub>4</sub>/ZnO S-scheme photocatalysts for improved H<sub>2</sub>O<sub>2</sub> preparation, *Chin. J. Catal.* 53 (2023) 123–133, [https://doi.org/10.1016/s1872-2067\(23\)64514-0](https://doi.org/10.1016/s1872-2067(23)64514-0).
  - [18] H. Hirakawa, S. Shiota, Y. Shiraishi, H. Sakamoto, S. Ichikawa, T. Hirai, Au Nanoparticles supported on BiVO<sub>4</sub>: effective inorganic photocatalysts for H<sub>2</sub>O<sub>2</sub> production from water and O<sub>2</sub> under visible light, *ACS Catal.* 6 (2016) 4976–4982, <https://doi.org/10.1021/acscatal.6b01187>.
  - [19] K. Wang, M. Wang, J. Yu, D. Liao, H. Shi, X. Wang, H. Yu, BiVO<sub>4</sub> microparticles Decorated with Cu@Au core-shell nanostructures for photocatalytic H<sub>2</sub>O<sub>2</sub> production, *ACS Appl. Nano Mater.* 4 (2021) 13158–13166, <https://doi.org/10.1021/acsnm.1c02688>.
  - [20] Z. Yang, J. Wang, Photo-Fenton degradation of sulfamethazine using self-assembled CdS nanorods with in-situ production of H<sub>2</sub>O<sub>2</sub> at wide pH range, *Chem. Eng. J.* 450 (2022) 138024, <https://doi.org/10.1016/j.cej.2022.138024>.
  - [21] M. Qian, X.L. Wu, M. Lu, L. Huang, W. Li, H. Lin, J. Chen, S. Wang, X. Duan, Modulation of charge trapping by island-like single-atom cobalt catalyst for enhanced photo-Fenton-like reaction, *Adv. Funct. Mater.* 33 (2023) 2208688, <https://doi.org/10.1002/adfm.202208688>.
  - [22] S. Pourabrahimi, M. Pirooz, Synthesis of a novel freestanding conjugated triazine-based microporous membrane through superacid-catalyzed polymerization for superior CO<sub>2</sub> separation, *Chem. Eng. J. Adv.* 11 (2022) 100315, <https://doi.org/10.1016/j.cej.2022.100315>.
  - [23] Y. Liu, B. Li, Z. Xiang, Pathways towards boosting solar-driven hydrogen evolution of conjugated polymers, *Small* 17 (2021) 2007576, <https://doi.org/10.1002/smll.202007576>.
  - [24] S. Gao, X. Wang, C. Song, S. Zhou, F. Yang, Y. Kong, Engineering carbon-defects on ultrathin g-C<sub>3</sub>N<sub>4</sub> allows one-pot output and dramatically boosts photoredox catalytic activity, *Appl. Catal. B: Environ.* 295 (2021) 120272, <https://doi.org/10.1016/j.apcatb.2021.120272>.
  - [25] M. Zhou, G. Dong, F. Yu, Y. Huang, The deep oxidation of NO was realized by Sr multi-site doped g-C<sub>3</sub>N<sub>4</sub> via photocatalytic method, *Appl. Catal. B: Environ.* 256 (2019) 117825, <https://doi.org/10.1016/j.apcatb.2019.117825>.
  - [26] M. Zhou, G. Dong, J. Ma, F. Dong, C. Wang, J. Sun, Photocatalytic removal of NO by intercalated carbon nitride: the effect of group IIA element ions, *Appl. Catal. B: Environ.* 273 (2020), <https://doi.org/10.1016/j.apcatb.2020.119007>.
  - [27] X. Wu, H. Fan, W. Wang, L. Lei, X. Chang, L. Ma, Multiple ordered porous honeycombed g-C<sub>3</sub>N<sub>4</sub> with carbon ring in-plane splicing for outstanding photocatalytic H<sub>2</sub> production, *J. Mater. Chem. A* 10 (2022) 17817–17826, <https://doi.org/10.1039/d2ta04163d>.
  - [28] S. Yang, Q. Wang, Q. Wang, G. Li, T. Zhao, P. Chen, F. Liu, S.-F. Yin, Linkage engineering mediated carriers transfer and surface reaction over carbon nitride for enhanced photocatalytic activity, *J. Mater. Chem. A* 9 (2021) 21732–21740, <https://doi.org/10.1039/d1ta03813c>.
  - [29] J. Xia, N. Karjule, G. Mark, M. Volokh, H. Chen, M. Shalom, Aromatic alcohols oxidation and hydrogen evolution over  $\pi$ -electron conjugated porous carbon nitride rods, *Nano Res.* 15 (2022) 10148–10157, <https://doi.org/10.1007/s12274-022-4717-4>.
  - [30] W. Che, W. Cheng, T. Yao, F. Tang, W. Liu, H. Su, Y. Huang, Q. Liu, J. Liu, F. Hu, Z. Pan, Z. Sun, S. Wei, Fast photoelectron transfer in (C<sub>ring</sub>)-C<sub>3</sub>N<sub>4</sub> plane heterostructural nanosheets for overall water splitting, *J. Am. Chem. Soc.* 139 (2017) 3021–3026, <https://doi.org/10.1021/jacs.6b11878>.
  - [31] Y. Guo, Q. Zhou, J. Nan, W. Shi, F. Cui, Y. Zhu, Perylene-tetracarboxylic acid nanosheets with internal electric fields and anisotropic charge migration for photocatalytic hydrogen evolution, *Nat. Commun.* 13 (2022) 2067, <https://doi.org/10.1038/s41467-022-29826-z>.
  - [32] Z. Zhang, X. Chen, H. Zhang, W. Liu, W. Zhu, Y. Zhu, A highly crystalline perylene imide polymer with the robust built-in electric field for efficient photocatalytic water oxidation, *Adv. Mater.* 32 (2020) 1907746, <https://doi.org/10.1002/adma.201907746>.
  - [33] X. Xu, L. Meng, J. Zhang, S. Yang, C. Sun, H. Li, J. Li, Y. Zhu, Full-spectrum responsive naphthalimide/peryrene diimide with a giant internal electric field for photocatalytic overall water splitting, *Angew. Chem. Int. Ed.* 63 (2023) e202308597, <https://doi.org/10.1002/anie.202308597>.
  - [34] J. Yang, J. Jing, W. Li, Y. Zhu, Electron donor-acceptor interface of TPPS/PDI boosting charge transfer for efficient photocatalytic hydrogen evolution, *Adv. Sci.* 9 (2022) e2201134, <https://doi.org/10.1002/adv.202201134>.
  - [35] X. Xu, S. Dai, S. Xu, Q. Zhu, Y. Li, Efficient photocatalytic cleavage of lignin models by a soluble perylene diimide/carbon nitride S-scheme heterojunction, *Angew. Chem. Int. Ed.* 62 (2023) e202309066, <https://doi.org/10.1002/anie.202309066>.
  - [36] L. Yang, G. Dong, D.L. Jacobs, Y. Wang, L. Zang, C. Wang, Two-channel photocatalytic production of H<sub>2</sub>O<sub>2</sub> over g-C<sub>3</sub>N<sub>4</sub> nanosheets modified with perylene imides, *J. Catal.* 352 (2017) 274–281, <https://doi.org/10.1016/j.jcat.2017.05.010>.
  - [37] L. Yang, P. Wang, J. Yin, C. Wang, G. Dong, Y. Wang, W. Ho, Engineering of reduced graphene oxide on nanosheet-g-C<sub>3</sub>N<sub>4</sub>/peryrene imide heterojunction for enhanced photocatalytic redox performance, *Appl. Catal. B: Environ.* 250 (2019) 42–51, <https://doi.org/10.1016/j.apcatb.2019.02.076>.
  - [38] Y. Li, Z. Jiang, G. Dong, W. Ho, Construction and activity of an all-organic heterojunction photocatalyst based on melem and pyromellitic dianhydride, *ChemSusChem* 15 (2022) e202200477, <https://doi.org/10.1002/cssc.202200477>.
  - [39] H. Chen, W. Zeng, Y. Liu, W. Dong, T. Cai, L. Tang, J. Li, W. Li, Unique MIL-53(Fe)/PDI supermolecule composites: Z-scheme heterojunction and covalent bonds for uprating photocatalytic performance, *ACS Appl. Mater. Interfaces* 13 (2021) 16364–16373, <https://doi.org/10.1021/acsmi.1c01308>.
  - [40] Z. Jiang, G. Dong, R. Wang, C. He, C. Wang, J. Sun, Enhanced interface charge transfer of Z-scheme photocatalyst by Br substitution at the bay position in perylene tetracarboxylic diimide, *Sol. RRL* 4 (2020) 2000303, <https://doi.org/10.1002/solr.202000303>.
  - [41] Y. Shi, Q. Zhao, J. Li, G. Gao, J. Zhi, Onion-like carbon-embedded graphitic carbon nitride for enhanced photocatalytic hydrogen evolution and dye degradation, *Appl. Catal. B: Environ.* 308 (2022) 121216, <https://doi.org/10.1016/j.apcatb.2022.121216>.
  - [42] X. Zhang, T. Wu, C. Yu, R. Lu, Ultrafast interlayer charge separation, enhanced visible-light absorption, and tunable overpotential in twisted graphitic carbon nitride bilayers for water splitting, *Adv. Mater.* 33 (2021) 2104695, <https://doi.org/10.1002/adma.202104695>.
  - [43] R. Tang, H. Zeng, C. Feng, S. Xiong, L. Li, Z. Zhou, D. Gong, L. Tang, Y. Deng, Twisted C-TiO<sub>2</sub>/PCN S-scheme heterojunction with enhanced  $n \rightarrow \pi^*$  electronic excitation for promoted piezophotocatalytic effect, *Small* 19 (2023) 2207636, <https://doi.org/10.1002/smll.202207636>.
  - [44] Q. Wang, J. Cao, X. Luo, S. Yang, F. Liu, P. Chen, S.-F. Yin, Steering rigidified nonplanar conjugation based perylene diimide supramolecular for enhancing photocatalytic activity, *Mater. Today* 61 (2022) 22–29, <https://doi.org/10.1016/j.mattod.2022.10.024>.
  - [45] X. Wu, B. Hu, D. Li, B. Chen, Y. Huang, Z. Xie, L. Li, N. Shen, F. Yang, W. Shi, M. Chen, Y. Zhu, Polymer photocatalysts containing segregated  $\pi$ -conjugation units with electron-trap activity for efficient natural-light-driven bacterial inactivation, *Angew. Chem. Int. Ed.* 62 (2023) e202313787, <https://doi.org/10.1002/anie.202313787>.
  - [46] Y. Wang, M. Liu, F. Fan, G. Li, J. Duan, Y. Li, G. Jiang, W. Yao, Enhanced full-spectrum photocatalytic activity of 3D carbon-coated C<sub>3</sub>N<sub>4</sub> nanowires via giant interfacial electric field, *Appl. Catal. B: Environ.* 318 (2022) 121829, <https://doi.org/10.1016/j.apcatb.2022.121829>.
  - [47] J. Li, L. Cai, J. Shang, Y. Yu, L. Zhang, Giant enhancement of internal electric field boosting bulk charge separation for photocatalysis, *Adv. Mater.* 28 (2016) 4059–4064, <https://doi.org/10.1002/adma.201600301>.

- [48] Y. Zhang, D. Wang, W. Liu, Y. Lou, Y. Zhang, Y. Dong, J. Xu, C. Pan, Y. Zhu, Create a strong internal electric-field on PDI photocatalysts for boosting phenols degradation via preferentially exposing  $\pi$ -conjugated planes up to 100, *Appl. Catal. B: Environ.* 300 (2022) 120762, <https://doi.org/10.1016/j.apcatb.2021.120762>.
- [49] J. Wang, X. Gu, H. Ma, Q. Peng, X. Huang, X. Zheng, S.H.P. Sung, G. Shan, J.W. Y. Lam, Z. Shuai, B.Z. Tang, A facile strategy for realizing room temperature phosphorescence and single molecule white light emission, *Nat. Commun.* 9 (2018) 2963, <https://doi.org/10.1038/s41467-018-05298-y>.
- [50] J. Wang, W. Shi, D. Liu, Z. Zhang, Y. Zhu, D. Wang, Supramolecular organic nanofibers with highly efficient and stable visible light photooxidation performance, *Appl. Catal. B: Environ.* 202 (2017) 289–297, <https://doi.org/10.1016/j.apcatb.2016.09.037>.
- [51] J. Sun, J. Bian, J. Li, Z. Zhang, Z. Li, Y. Qu, L. Bai, Z.-D. Yang, L. Jing, Efficiently photocatalytic conversion of CO<sub>2</sub> on ultrathin metal phthalocyanine/g-C<sub>3</sub>N<sub>4</sub> heterojunctions by promoting charge transfer and CO<sub>2</sub> activation, *Appl. Catal. B: Environ.* 277 (2020) 119199, <https://doi.org/10.1016/j.apcatb.2020.119199>.
- [52] P. Zhang, L. Li, J. Zhao, H. Wang, X. Zhang, Y. Xie, Elemental doping boosts charge-transfer excitonic states in polymeric photocatalysts for selective oxidation reaction, *Precis. Chem.* 1 (2023) 40–48, <https://doi.org/10.1021/prechem.2c00001>.
- [53] Z. Xiong, Z. Wang, L. Liu, M. Jiang, X. Zhang, Q. Zhu, H. Feng, Z. Qian, Breaking classic heavy-atom effect to achieve heavy-atom-induced dramatic emission enhancement of silole-based aiegens with through-bond and through-space conjugation, *Adv. Opt. Mater.* 9 (2021) 2101228, <https://doi.org/10.1002/adom.202101228>.